Rotorigami: A rotary origami protective system for robotic rotorcraft

Pooya Sareh[1,2]*, Pisak Chermprayong[1], Marc Emmanuelli[1], Haris Nadeem[1], Mirko Kovac[1]

Applications of aerial robots are progressively expanding into complex urban and natural environments. Despite remarkable advancements in the field, robotic rotorcraft is still drastically limited by the environment in which they operate. Obstacle detection and avoidance systems have functionality limitations and substantially add to the computational complexity of the onboard equipment of flying vehicles. Furthermore, they often cannot identify difficult-to-detect obstacles such as windows and wires. Robustness to physical contact with the environment is essential to mitigate these limitations and continue mission completion. However, many current mechanical impact protection concepts are either not sufficiently effective or too heavy and cumbersome, severely limiting the flight time and the capability of flying in constrained and narrow spaces. Therefore, novel impact protection systems are needed to enable flying robots to navigate in confined or heavily cluttered environments easily, safely, and efficiently while minimizing the performance penalty caused by the protection method. Here, we report the development of a protection system for robotic rotorcraft consisting of a free-to-spin circular protector that is able to decouple impact yawing moments from the vehicle, combined with a cyclic origami impact cushion capable of reducing the peak impact force experienced by the vehicle. Experimental results using a sensor-equipped miniature quadrotor demonstrated the impact resilience effectiveness of the Rotary Origami Protective System (Rotorigami) for a variety of collision scenarios. We anticipate this work to be a starting point for the exploitation of origami structures in the passive or active impact protection of robotic vehicles.

INTRODUCTION

The emergence of rotorcraft aerial robots, popularly known as drones, offers major opportunities for applications in various areas, such as environmental sensing, sampling, and surveillance. Although the potential uses of flying robots are increasing, flying in complex, constrained environments still remains a challenge. Environments with several potential collision surfaces prove to be major limitations for unmanned aerial operations. To date, research into drone adap-tation to cluttered environments has taken two different routes: (i) obstacle detection and avoidance (*1*–*5*) and (ii) mechanical impact resilience (*6*–*18*). Conventional approaches are largely focused on obstacle avoidance by using sensors to map the environment and potential collision surfaces. State-of-the art obstacle-avoidance systems have their basis in either vision-aided techniques (*19*–*27*), such as optical flow (*28*–*30*), or distance sensors exploiting radar (*31*, *32*), lidar (*33*), and sonar (*34*–*36*) technologies. A widely used obstacle detection and avoidance method is simultaneous localiza-tion and mapping, which builds an accurate map of obstacles by using high-precision onboard sensors (*37*–*44*). Other effectively demonstrated methods include collision-recovering controllers along with simple motion planners, enabling robots to navigate without complete knowledge of their surroundings. This technique allows aerial vehicles to fly in dark, Global Positioning System–- denied environments (*45*).

Mechanical impact resilience is an alternative approach to impact protection. It seeks to cope with collisions rather than to avoid them, which can also complement avoidance-based methods. It is based on the fact that most conventional flying platforms are generally unable to sustain flight after a collision with a surface, because the disturbance from the impact will likely cause a loss of control and lead to a crash. Traditional drones are not equipped with any impact resilience systems, with collisions often causing failure in the major components of the vehicle. Oblique collisions will also cause an additional yawing moment around the vehicle's center of mass, possibly leading to instabilities, further collisions, and crashes, which generally include high impact forces and potential damage to the vehicle. Commercially available mechanical protection concepts are not sufficiently effective and are often based on rigid components that do not mitigate collision forces. For example, propeller guards made of expanded/extruded polystyrene foam (EPS/XPS) are used as a lightweight and inexpensive solution for the protection of commercial multirotor drones. However, because EPS and XPS are both rigid materials with poor elastic behavior (*46*, *47*), they are unable to properly cushion impact forces in a recoverable manner.

Collision-resilient robots aim to increase the robustness of flight operations and can be deployed where collisions are unavoidable. Advanced mechanical concepts have been developed to tackle this problem innovatively by mitigating the translational and rotational effects of collisions on the flying platform. However, in general, these concepts are heavy and cumbersome, severely limiting the flight time and the capability of flying in constrained and narrow spaces. As an example, GimBall (*7*) outstandingly reduced the impact of friction forces on the attitude of the flying platform but imposed considerable penalties on flight time, versatility, and transport-ability of the vehicle. Moreover, it did not cushion impact forces; thus, normal collisions still led to high loads on the vehicle and the colliding object.

Mitigating the impact forces in both normal and oblique collisions is a major challenge, especially for very small vehicles for which substantial payload constraints prevent the possibility of

[1]Aerial Robotics Laboratory, Department of Aeronautics, Imperial College London, South Kensington Campus, SW7 2AZ London, UK. [2]Division of Industrial Design, School of Engineering, University of Liverpool, London Campus, EC2A 1AG London, UK.
*Corresponding author. Email: pooya.sareh@liverpool.ac.uk

using large and heavy protective structures. Origami engineering can be a solution to address this structural design challenge. Over the past decade, origami (the traditional Japanese art of paper folding) has found numerous novel applications in various areas of robotics (*48*–*59*). Because of the wide range of applications of origami engineering, the structural (*60*, *61*), acoustic (*62*, *63*), and thermal (*64*) properties of origami- inspired structures and metamaterials have been of great interest to scientists and engineers. For example, origami structures have been used as impact protection concepts (*65*–*67*) for potential applications such as novel crash boxes in automotive industry (*68*, *69*). Furthermore, biological morphing structures, such as insect and bird wings, have inspired the development of origami patterns, typically finite folding patterns with a small number of vertices, as concepts for mechanical flapping wings (*70*–*73*).

In this paper, we report the design and development of a lightweight and cost-effective mechanical impact protection system for miniature quadrotor aerial platforms, and we compare it with traditional rigid propeller protection concepts. The proposed design allows these platforms to remain stable after a variety of normal and oblique collisions that are intolerable with rigid protectors. Further-more, because collisions would become more tolerable and because flight speed through complex environments can be limited due to sensing and compensation time scales, the proposed design may allow locomotion at potentially higher speeds. Last, impact avoid-ance strategies can be complemented with the impact resilient na-ture of the proposed design, leading to a potential reduction in the weight and complexity of the employed onboard sensors.

RESULTS

Analysis, design, and development

The principle of individual propeller guards (Fig. 1A) is currently the most common protection accessory for multicopters. Although several variations of this configuration exist (including four connected and stringed guards), the principle drawback remains the same: Be-cause the guard is fixed to the drone, the moments induced due to the arising tangential force F_t and normal force F_n both contribute to the yawing moment about the center of the drone that causes flight instability.

As an improvement on the common individual protectors, we aimed to develop a mechanical system that withstands collisions effectively and can be integrated into existing flying platforms. A slightly improved variation to be considered in this conceptual analysis is the decoupled individual propeller guard (Fig. 1B): If the propeller guard was to rotate independently from the drone, assum-ing a decoupled system is implemented, then the moment arm due to F_t would be reduced. However, this configuration has the same low resilience against the yawing moment induced by the normal force as in the previous configuration.

The advantage of a fixed universal (protecting all propellers) protector (Fig. 1C) over individual guards for a multicopter is that, in the case of a universal guard, the normal force, F_n, does not produce any yawing moment around the center of mass of the multi-copter, assuming that the guard rotates around its center of mass (*8*, *74*). The final and most advantageous design considered is a decoupled universal protector (Fig. 1D). Theoretically, assuming that

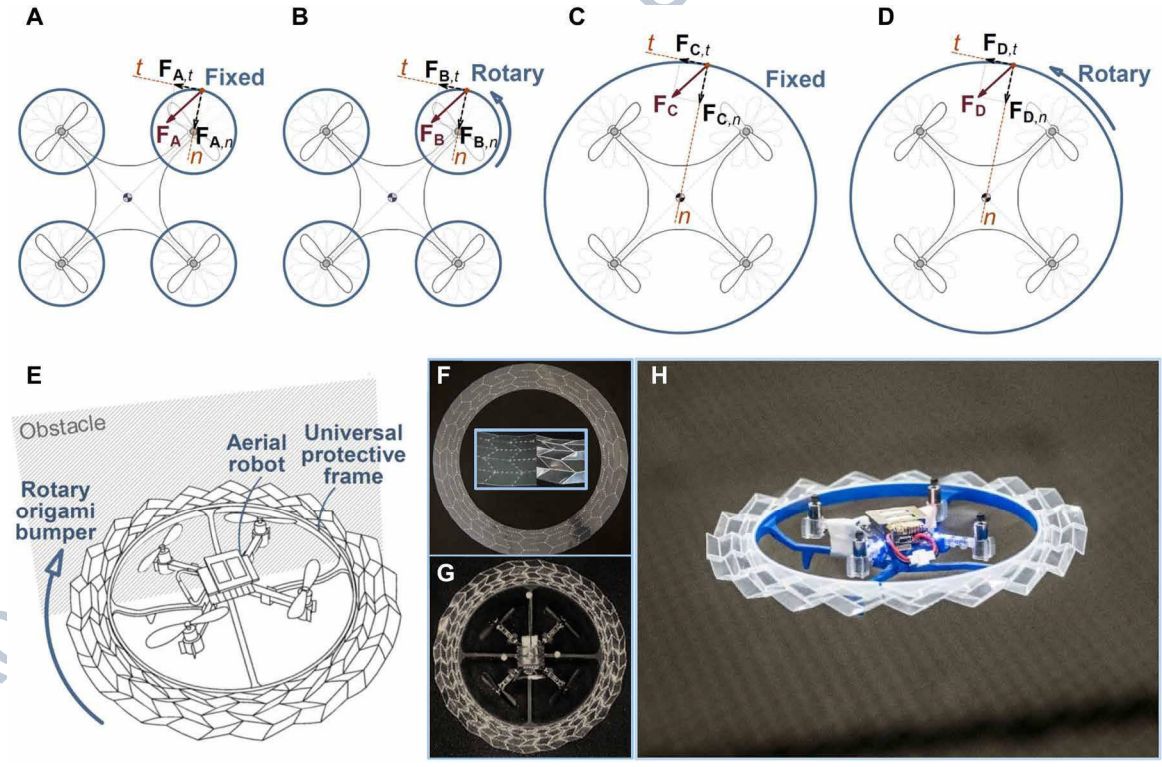

Fig. 1. Conceptual analysis, design, and development of Rotorigami for quadcopters. (**A** to **D**) Graphical representations of four mechanical protection systems: (**A**) fixed individual propeller protector, (**B**) rotary individual propeller protector, (**C**) fixed universal protector, and (**D**) rotary universal protector. (**E**) Rotary universal protector with origami cushion. (**F**) Laser-cut pattern and its detailed view before and after folding along its perforated crease lines. (**G**) A miniature quadcopter equipped with Rotorigami (Rotary Origami Protective System) in a plan view and (**H**) in flight.

the center of the universal protector is coincident with the center of mass of the drone and that the friction in rotational joints between the platform and the protector is negligible, a decoupled universal protector will eliminate all yawing moments arising from the collision.

In addition to moment decoupling as a first strategy, a second strategy to enhance the impact robustness of aerial robots is to minimize the peak collision force experienced by the platform. Given the weight of the protector as a main challenge and to realize the notion of an ultralightweight impact cushion, we demonstrated the functionality of an origami impact protector made of a very thin plastic sheet (Fig. 1, E to H). Among a large variety of origami patterns, the Miura-ori (*75–78*) is perhaps the most widely used tessellation in engineering design as a result of its manufacturing simplicity, geometric versatility, and desirable functional properties. In addition to free-form variations (*79*), several studies have pro-posed symmetric derivatives for this pattern that can alter both the form and the functionality of the original pattern [see, e.g., (*80*, *81*)]. Variations with finite symmetry groups include several descendants with rosette symmetry [i.e., two-dimensional point groups (*82*)], including cyclic and dihedral descendants. By using a group-- theoretic framework (*83*), we have designed an extensive family of isomorphic (*84–86*) and nonisomorphic (*87*, *88*) wallpaper-- symmetric (*89*) variations for this pattern (Fig. 2A). Whereas wallpaper derivatives of the pattern are useful as concepts for axial springs and crash boxes, rosette variations can be used as radial springs and shock absorbers due to their radial transformation. On the basis of a simple cyclic variation of the Miura-ori (Fig. 2B) (*90 –93*), which allows a straightforward manufacturing process, we developed a protector capable of reducing the peak force expe-rienced by the vehicle in a collision.

Modeling the cyclic origami ring as a function of five geometric parameters (Fig. 3A) enabled us to produce an array of different models that served as inputs to finite element analysis (FEA). The origami ring was a thin-walled structure (*94*), and the miniature drone was a low-speed, lightweight vehicle. As a result, to choose a suitable design for the ring, we adapted the quasi-static FEA simu-lation method, which is widely used for evaluating impacts of thin-walled structures (*95–100*). The simulations involved displacing a rigid plate toward the center of the origami structures (see the Supplementary Materials for details). By performing a series of identical simulations on origami structures with varying geometric parameters, it was possible to carry out a comparative analysis, relating those parameters to the stiffness and energy absorption capabilities of the structures under compression.

The two parameters that affect the overall geometry of the structure are the number of radial segments, n, and the pattern angle, , which composed a set of models to be simulated (Fig. 3C) . After processing the FEA results, the structural behavior of each model was determined (for details, see the "Parametric comparative analysis of origami structures" section in the Supplementary Materials). Specific outputs were extracted from the resulting force-versus-- displacement curves to characterize the structural performance of each model for the purpose of choosing a suitable design. These outputs were (i) the elastic energy (temporarily) absorbed by the structure until it slips out of plane, (ii) the peak reaction force during compression, and (iii) the mass of the structure. It is desirable to have a lightweight protective structure with high elastic energy absorption capacity, that is, a structure with high specific elastic energy (elastic energy per unit mass). Furthermore, to minimize the risk of damage to the vehicle, the protective ring must have a rela-tively low peak reaction force during compression.

The results showed that if the projected height of the structure, H, on the compressing plate is small in proportion to its width, W (Fig. 3B), then it will be more unstable (i.e., prone to elastic buck-ling). By increasing the pattern angle of the structure, it not only gets thinner (in proportion to its height), but there are also fewer fold lines per unit width, and the facets are each elongated in the direction of the force applied. The structure therefore becomes less stiff and more unstable. Moreover, we noticed that the energy absorbed for low pattern angles is also low (fig. S5). In this case, the stiffness is so high that the structure slips quickly out of plane due to a high applied force before absorbing a considerable amount of energy. Furthermore, analyses of the stiffness and the energy ab-sorption capabilities of the model implied that, although increasing the number of radial segments makes the structure stiffer, it also makes the structure less stable. Last, as can be seen in fig. S7, reduc-ing the pattern angle and increasing the number of radial segments create the most lightweight structures. The specific energy analysis (fig. S8) indicated that, in general, a more desir-able design can be achieved by choosing a pattern angle of 30°. In addition, it was observed that, as a general trend, increasing the number of radial segments increases the peak reaction force.

In addition to the structural design considerations and to provide a well--suited design for the intended application, we took into account the manufacturability of the structure at small scale (to suit the palm-sized flying robot used in this study) as an extra design consideration. Although increasing n at a con-stant would create a more desirable ring in terms of structural performance, it would also make the hand-folding pro-cess increasingly difficult. This is due to

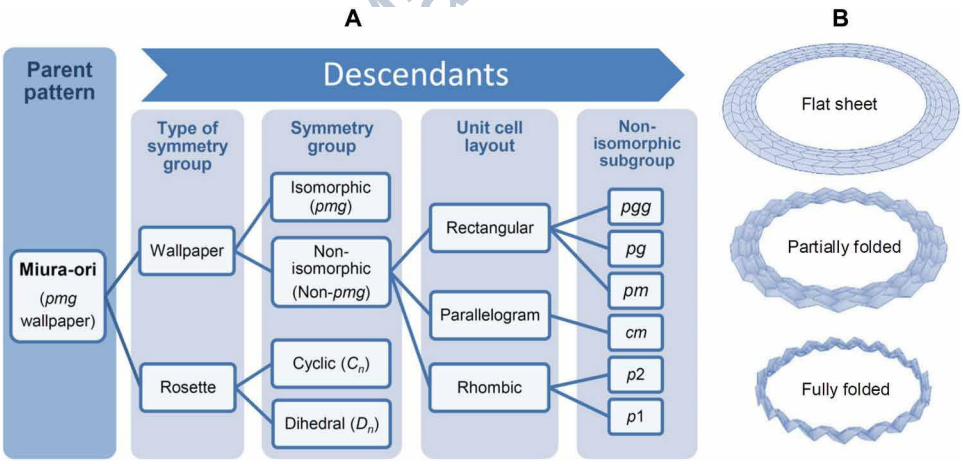

Fig. 2. Concept selection for a circular variation of the Miura-ori and its folding transformation. (**A**) Family tree displaying the symmetric descendants of the Miura fold pattern. (**B**) Three states in the radial transformation of a cyclic variation of the Miura-ori.

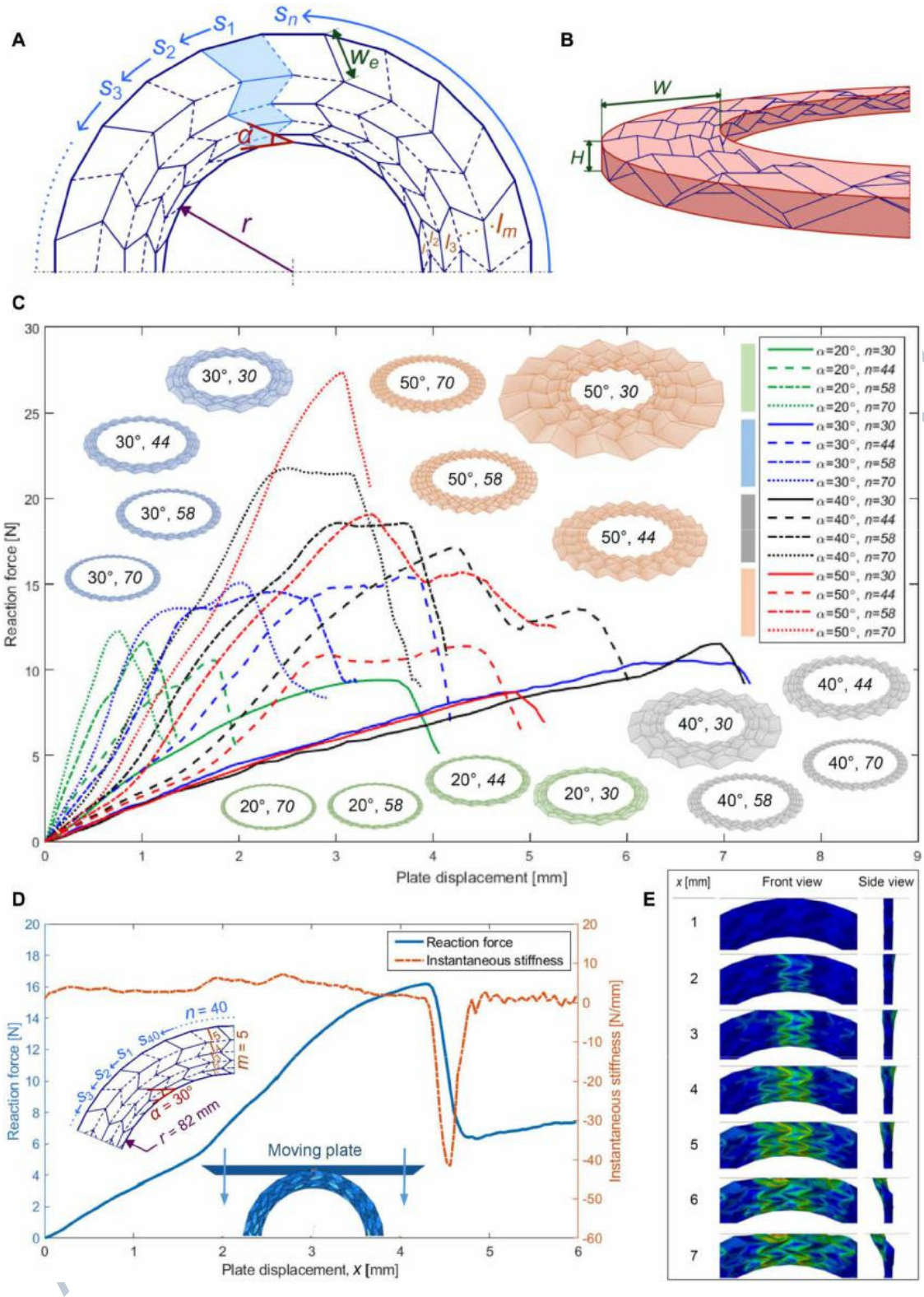

Fig. 3. Geometric modeling and structural design optimization of the cyclic Miura-ori. (**A**) Half of a typical cyclic descendant of the Miura fold pattern and its geometric parameters: n, number of radial segments (s_1 to s_n); , pattern angle; r, inner radius; m, number of concentric layers (l_1 to l_m); $\bar{w} = w_e/w_u$, normalized width of external facets, where w_e is the external facets width and w_u is the unchanged facets width for the pattern sequence. Mountain and valley folds are represented by solid and dashed lines, respectively. (**B**) A ring-shaped solid (mathemati-cally speaking, a cylindrical annulus) fitting around an ex-ample model. (**C**) Sixteen ori-gami rings and output data from quasi-static FEA simula-tions on models with varying parameters and n, whereas $\bar{w} = 1$. As the number of radial segments on the pattern is increased, so is the stiffness of the structure. However, this also has the effect of shorten-ing the time during which the structure is stable under com-pression before it slips out of plane. (**D**) Reaction force ver-sus displacement curve for the selected design (illustrated on the left part of the figure) and its gradient, which is a measure of the stiffness of the structure. The simulation set-up is depicted on the bottom part of the panel. (**E**) Front and side views of the FEA simula-tion for the compression of the selected structure.

two reasons. First, increasing n proportionally increases the number of internal vertices of the structure. This not only increases the number of lines to be folded but also makes the facets progressively smaller. Keeping in mind the limits of manual fabrication, as the facets become smaller, folding the pattern without damage to internal facets poses a substantial fabrication challenge. As a result, for the given size of the ring, we manufactured a structure with $n = 40$ as a reasonable trade-off between structural performance and manufacturability.

On the basis of the abovementioned considerations, we chose a suitable design with = 30°, $n = 40$, $r = 82.0$ mm, $m = 5$, and $w_e/w_u = 0.8$,

where r is the inner radius, m is the number of concentric layers (l_1 to l_m), and w_e/w_u is the normalized width of external facets (w_e is the exter-nal facets width, and w_u is the unchanged facets width for the pat-tern sequence) (see the left-hand side of Fig. 3D). As expected, the selected structure was observed to slip out of plane after an initial planar contraction in the FEA simulation (see the bottom part of Fig. 3D and the Supplementary Materials for the simulation setup). The force-versus-displacement curve (Fig. 3D) confirms this slip in the form of a sudden drop in the reaction force on the plate after a displacement of x = 4.33 mm. The first derivative of this curve indi-cates two punctuated increases in its gradient at x = 1.74 mm and x = 2.47 mm. These points correspond to the moments when external vertices come into contact with the plate (Fig. 3E). This triggers the facets and fold lines that are linked to these vertices to experience bending, which stiffens the structure. However, the gradient then slowly decays until the slip point. Because the structure is not perfectly symmetrical about its horizontal plane, it will eventually buckle as the force imposed on it increases.

Collision experiments and analyses

To investigate the capabilities of the proposed protective concept, we carried out impact experiments with a miniature multirotor aerial robot. The following are the four universal design configura-tions that were tested for their impact resilience performance: (i) fixed naked (Fig. 1C), (ii) rotary naked (Fig. 1D), (iii) fixed origami-- protected [Fig. 1E; without rotational degrees of freedom (DOF)], and (iv) rotary origami-protected (Fig. 1E; with rotational DOF) universal protectors. The peak impact force and angular speed of these design configurations were measured and analyzed to com-pare their corresponding impact protection qualities in normal and oblique collisions. In these experiments, pendulum swing tests were performed by using the quadcopter equipped with an inertial mea-surement unit (IMU) module as a pendulum mass. A maximum velocity of 1.2 m/s at the lowest point of the pendulum swing was set as a typical target velocity to simulate a horizontal collision to a sur-face. The masses of the robot naked and with the origami protector were not the same due to the added weight of the origami structure; the origami-protected configurations had a mass of 53.0 g, whereas the naked configurations were both 48.5 g. Hence, the impact forces were calculated from the actual mass of each design configuration. The impact surfaces were switched between smooth (acrylic glass) and rough (sandpaper with ISO Grit P80) to determine the effect of the friction coefficient of hitting surfaces. The pendulum string held the drone at certain positions to simulate impacts at differ-ent angles of collision with respect to the colliding surface: 30°, 60°, and 90° (normal collision). For each collision scenario, the average values of force and angular speed from five tests were plotted on the basis of 30 samples at a 600-Hz sampling frequency, with peak forces aligned to show relevant force and angular speed profiles be-fore and after impact. Each line plot also contains its minimum and maximum occurred values in the sample data sets to show the range of the data (Figs. 4 and 5). The next two sections present the analy-ses of the experimental results.

Impact-cushioning strategy: Naked versus origami-protected configurations

The collision duration in the origami- protected systems was ob-served to be notably longer than that of the naked systems, provid-ing a substantial level of impact cushioning. We began by comparing the impact protection quality between naked and origami--protected systems in a normal collision (movie S1). The force and angular speed profiles of both systems for each experiment setup are plotted in the same figure to aid visual comparison (Fig. 4 and table S1). The peak force reduction turned out to be around 30% for both fixed (Fig. 4, A and C) and rotary (Fig. 4, B and D) origami-protected systems when compared with the naked configurations.

The next study consisted of collisions at 60° (movie S2); given the fact that impacts at this angle are closer to normal rather than tan-gential collision, the normal component of the impact force was dominant. The peak force reduction by the origami structure in both fixed and rotary configurations was around 38% on average. Last, for impacts at 30° with respect to the collision surface, in which the tangential collision force was dominant, the peak force reduction was around 20%.

Moment-decoupling strategy: Fixed versus rotary configurations

To investigate the performance of the rotary configurations com-pared with the fixed ones, we plotted force and angular speed data in a way similar to the previous section. In this case, rather than comparing naked and origami-protected systems, data for the fixed and the rotary systems were plotted in the same graph for each ex-periment setup. The effect of the rotary concept on the reduction of rotational speed after impact was demonstrated in the 30° impact experiments (Fig. 5 and movie S3), where the tangential component of collision force was relatively large. As anticipated, every fixed protection system displayed considerably higher rotational speed after impact compared with the rotary systems. Specifically, the fixed protection systems were not effective against the rough surface in sliding collisions, because the average maximum angular speed for fixed naked and fixed origami-protected systems were recorded to be around 814 and 697 degrees per second (DPS), respectively. Although those values for the fixed protection system on the smooth surface were lower compared with those of the rough surface due to lower friction, they were still significantly high: around 392 and 579 DPS for fixed naked and fixed origami-protected systems, respectively. In contrast, the rotary systems effectively decoupled shear impact force, resulting in an average maximum angular speed of one order of magnitude smaller compared with those of the fixed protection systems in the collision scenarios above. In the 60° collision experi-ments, again, the rotary protection systems showed superior impact-- reduction performance in all tests: On average, a reduction in angular speed around 82% (fig. S13 and table S1) was achieved for the four collision scenarios by using the moment-decoupling strategy. In normal collisions, the fixed and rotary systems performed simi-larly as expected because of the dominance of the normal com-ponent of the collision force (fig. S14 and table S1).

DISCUSSION

By combining a ring-shaped origami structure and a passively ro-tating universal circular frame, we developed and demonstrated an effective protection system that could cushion impact to reduce the overall collision peak force experienced by the drone and decouple the induced yawing moment from the platform (Fig. 6A). Extensive experimental work in a range of impact angles on both smooth and rough surfaces demonstrated that the simultaneous exploitation of these two concepts is the most advantageous design configuration

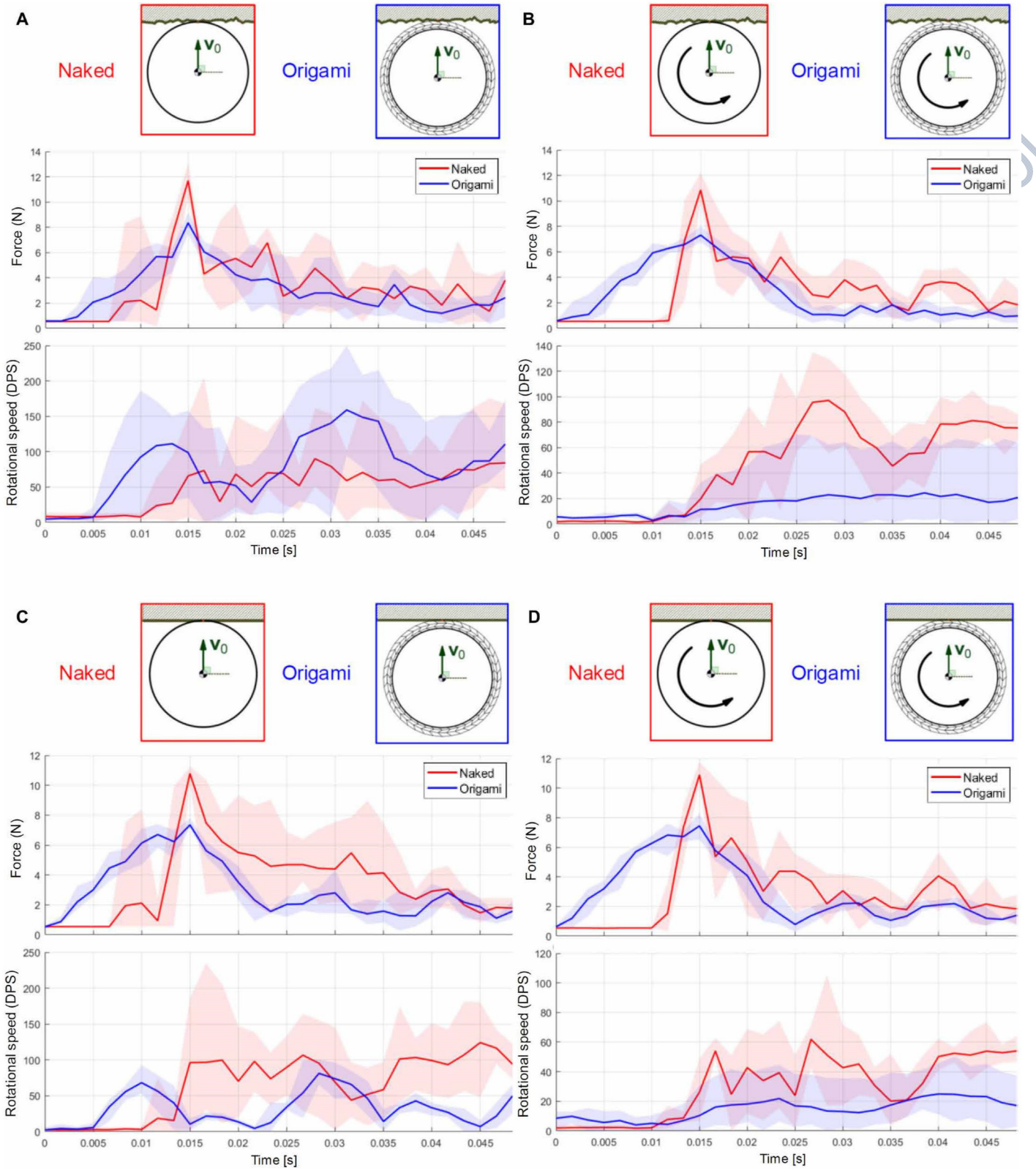

Fig. 4. Force and angular speed profiles in the normal collision (contact angle, 90°) at 1.2 m/s for the naked and origami-protected configurations on the rough and smooth surfaces. The design configuration and collision conditions related to each impact scenario are illustrated by icons above each graph. The shaded areas represent the range of data (from five trials) corresponding to each collision. (**A**) Rough surface with fixed protector. (**B**) Rough surface with rotary protector. (**C**) Smooth surface with fixed protector. (**D**) Smooth surface with rotary protector.

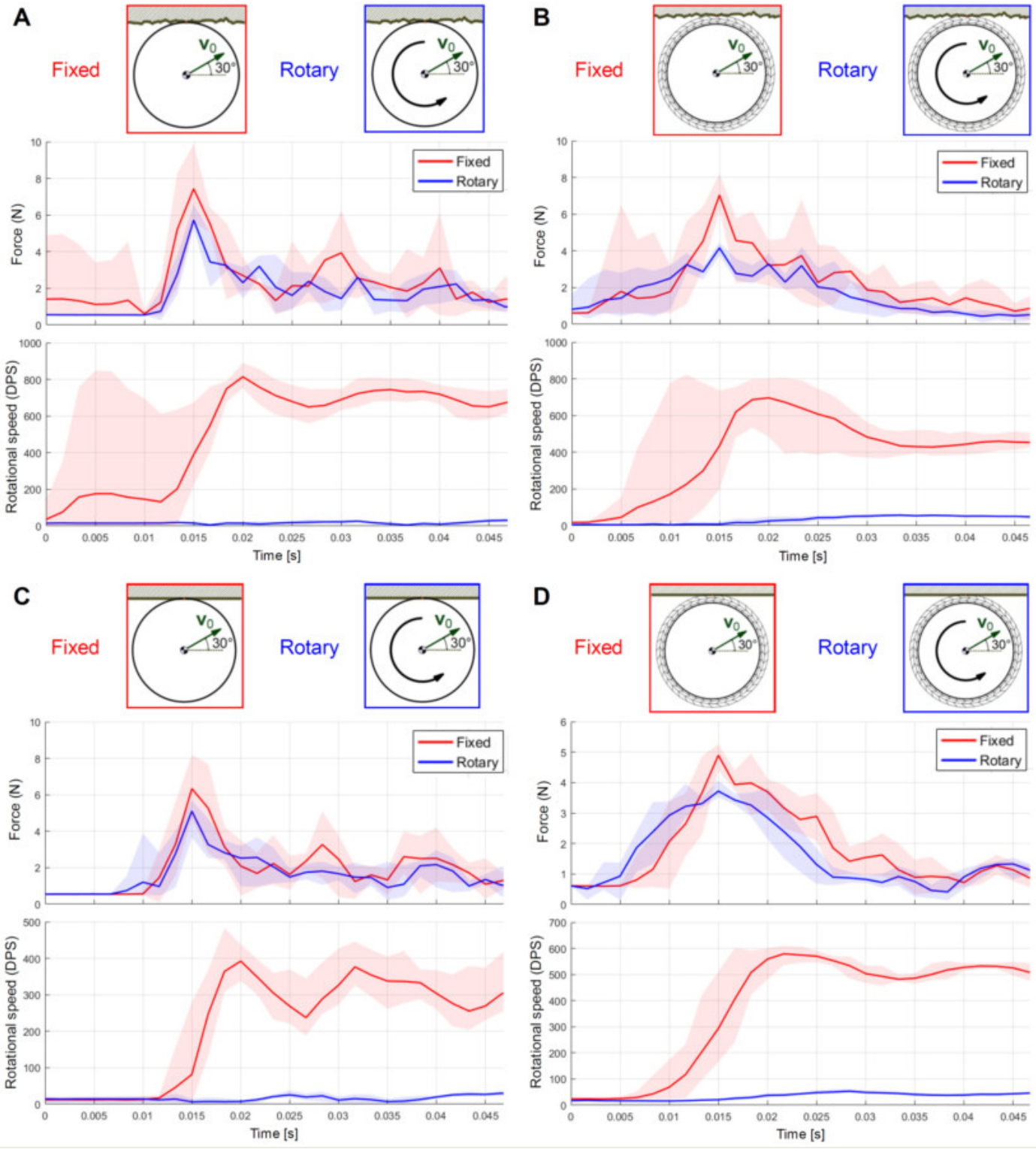

Fig. 5. Force and angular speed profiles at a contact angle of 30° and initial speed 1.2 m/s for fixed and rotary configurations on rough and smooth surfaces. The design configuration and collision conditions related to each impact scenario are illustrated by icons above each graph. The shaded areas represent the range of data (from five trials) corresponding to each collision. (**A**) Rough surface with naked protector. (**B**) Rough surface with origami protector. (**C**) Smooth surface with naked pro-tector. (**D**) Smooth surface with origami protector.

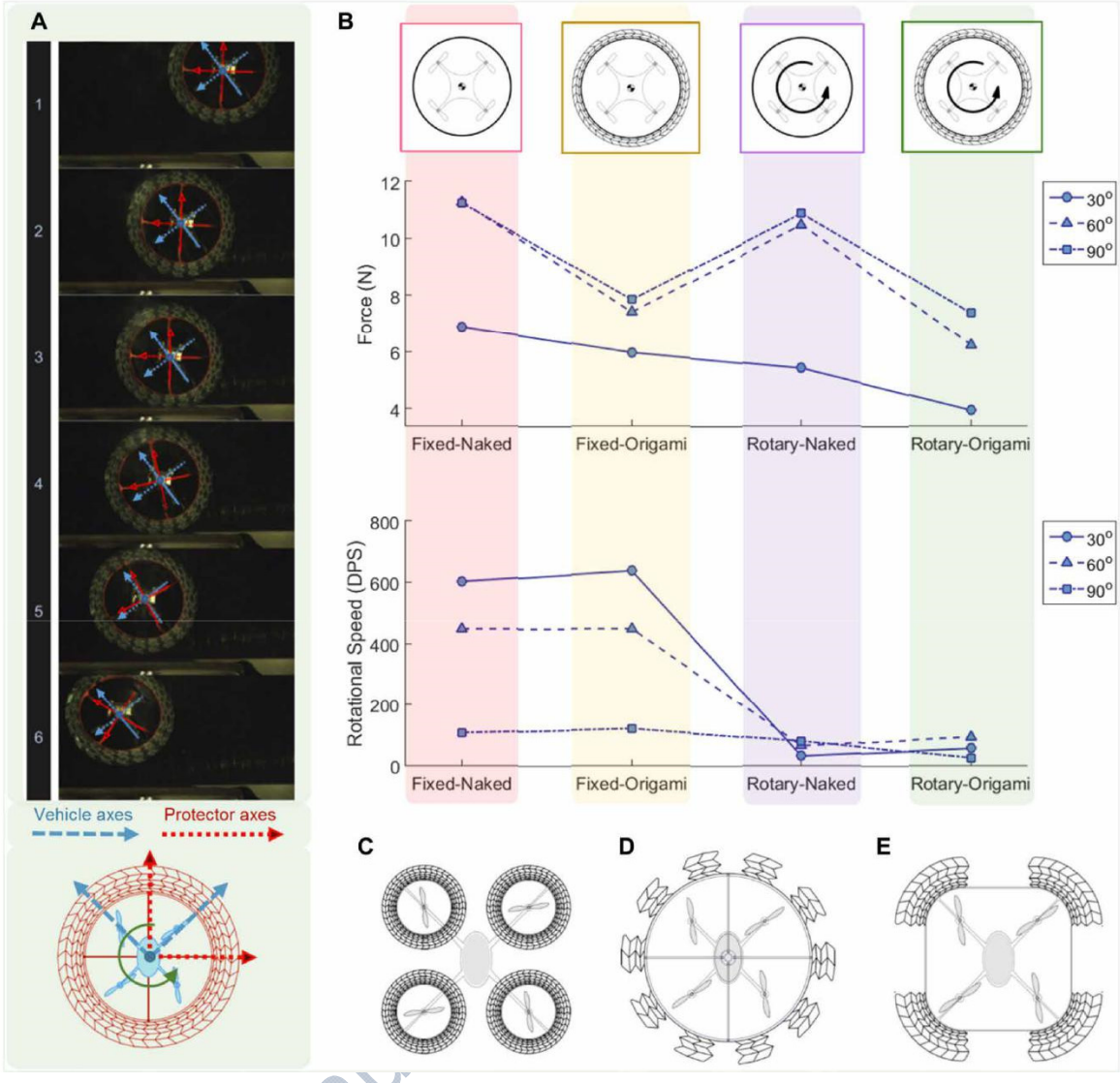

Fig. 6. Analysis of experimental results. (**A**) Snapshots from high-speed camera videos for an oblique collision with a rough surface at a contact angle of 30° for the origami-protected system in the rotary configuration. Although the protector axes (red) rotate significantly upon impact to the surface, the orientation of the vehicle body axes remains almost invariant. (**B**) Summary of all results (values averaged between rough and smooth surfaces) demonstrating that the Rotary-Origami (Rotorigami) configuration is the most advantageous design configuration in terms of the overall impact resilience quality. (**C** to **E**) A series of conceptual designs for origami-protected aerial robots.

in terms of the overall impact resilience quality (Fig. 6B). In summary, origami-protected systems offered about 30% improvement in the peak impact force reduction compared with naked-protection systems in all tested collision scenarios. By changing the material thickness and perforation settings on a laser or blade cutter, this protector can be fabricated with different levels of stiffness for diverse applications, providing a range of softness levels and therefore a range of peak force reduction capacities appropriate for various missions and environments. For example, for low-speed hovering around people and animals or in an area with delicate and fragile obstacles, the origami ring must be scored or perforated more deeply; this may provide a relatively soft protective structure that makes the vehicle safe to fly around vulnerable obstacles.

The concept motivates future research on the utility of origami structures for enhancing the impact resilience of aerial and ground robotic vehicles. Future research will also need to incorporate dynamic and aerodynamic flight studies of the proposed concept. An important note is that, although the universal protective configu-ration improves the collision resilience of the vehicle by improving its response to the impact-yawing moment, there is a pitching moment increase penalty due to the larger moment arm for the im-posed out-of-plane component of the impact force, compared with individual protective configuration. This increased pitching moment could cause the vehicle to tip over upon contact with the obstacle in the naked configurations. However, experiments showed (movies S1 and S4) that, by equipping the vehicle with an origami ring, the tendency of the vehicle to pitch is substantially decreased. This improved stability could be explained as the combination of three factors: First, the origami ring considerably increases the mass moment of inertia of the vehicle with respect to the pitch axis; second,

the aerodynamic resistance to pitch is larger for the origami--protected system due to its increased contact area; and finally, the peak impact force (and therefore its out-of-plane component) is smaller in the origami- protected configurations, leading to de-creased tendency to tip over upon impact.

Although this study was confined to a passive structure, it could be a starting point for developing advanced concepts with actively deployable origami structures capable of adjusting their stiffness for optimal contact with different surfaces. These structures could be fully folded (retracted) when the vehicle is not flying in a cluttered environment, that is, where it experiences a higher risk of collision to obstacles. This could lead to improved flight endurance. To enhance crash resilience, a second generation of this protective concept should include an active mechanism that protects the aerial robot in top and bottom collisions, without compromising the physical compactness of the vehicle. Furthermore, the same design principles can be extended and applied to other protected configu-rations, such as the individual propeller guards (Fig. 6C) and uni-versal frames with modular origami impact cushions (Fig. 6, D and E). Future research may consider advanced structural concepts and further optimization of the protective ring. This may include kirigami-inspired structures with cutout facets to decrease the struc-tural mass of the system while preserving an appropriate level of structural performance.

MATERIALS AND METHODS

Protective system fabrication and aerial platform selection

The impact-protection origami structure was folded manually from a 0.2-mm-thick laser-cut sheet of polypropylene (Fig. 1F). To facili-tate folding and to ensure the accurate geometric replication of the origami model, we engraved perforations along the fold lines of the pattern using a Versa CO_2 laser cutter (Universal Laser Systems PLS6.75). To change their depth and width, we engraved these fold line perforations by using different power settings on the laser cutter. Because low engraving power settings may create scores that do not cut through the entire thickness of the sheet, the mountain and valley fold lines were engraved separately on each side of the sheet. The plastic deformation created along the fold lines is an important ele-ment to consider when assessing the structural performance of the manufactured protection structure. The structure was assembled on a three-dimensionally printed acrylonitrile butadiene styrene plastic frame in the form of a cylindrical shell with a thickness of 1.1 mm. The palm-sized quadrotor Crazyflie 2.0 was chosen to be the testing platform. Its small size (92 mm × 92 mm × 29 mm) and reasonable payload capacity of up to 18 g ensured that the protection frame and the origami structure were fabricated on a small scale, thereby re-ducing complexities in their manufacturing processes. The small size and the limited payload of this platform also demonstrated the benefits of origami--inspired solutions as impact-protection struc-tures. These benefits include low weight and high design flexibility to achieve a desirable level of structural performance by perforating and folding an inexpensive plastic sheet.

Finite element simulations setup

The folded model was a three -dimensional shell object. When importing it into Abaqus FEA, we added thickness to it with the surface of the object as the mid-plane. This means that, whereas the geometry of the structure was accurately represented in these models, the nature of the fold lines (with perforations and plastic deformation) was not. Perforations and plastic deformation at the fold lines reduce the stiffness of the structure, which is very difficult to accurately represent in FEA simulations. However, the Abaqus models used in the finite element simulations were very useful for a comparative analysis to make a design decision. Because this study was only concerned with horizontal impact, the simulation involved displacing a vertical rigid plate toward the center of the protection structure. For the purpose of a comparative parametric analysis, it was important to be consistent in the choice of loads and boundary constraints imposed on the structure. The origami structures were meshed by using S4R shell elements. To analyze exclusively the structural behavior of the origami structure, we omitted the other components in the assembly (the quadrotor and the supportive frame) from the simulations and replaced them by a rigid body constraint on the innermost vertices of the origami structure. Figure S2B shows this constraint in Abaqus, where the vertices marked in red are parts of a fully constrained rigid body.

Collision experiments setup and data logging system

To obtain certain collision velocities, we used a simple energy conservation equation between potential and kinetic energy ($E = mgh = 0.5\ mv^2$) to calculate the required height at a pendulum releasing point, where E is the total amount of mechanical energy, m is the pendulum mass, h is the height of the pendulum from the releasing point to the point of impact, and v is the velocity upon impact to the wall. An electromagnet was used to hold and release the vehicle precisely to make sure that each collision has the same initial velocity and initial orientation for each testing configuration (fig. S15A).

We integrated a miniature data logging system into the aerial robot for the measurement of dynamic variables. The MinIMU-9 V5 with LSM6DS33 (featuring a three-axis accelerometer and a three-- axis gyroscope) and LIS3MDL (featuring a three-axis magnetometer) was chosen as an IMU due to its small size, high data rate, and broad range of sensing. The Adafruit Feather M0 data logger with micro secure digital (SD) card module was programmed and connected to work with the above sensor. The connection diagram was shown in fig. S15B. An Arduino library for LSM6 devices from Pololu was modified by using the SdFat library to increase micro SD card writing speed (*101*, *102*). An Ultra Micro secure digital high capacity (SDHC) card with UHS-I bus interface was tested with the data logger in terms of sensor data writing speed. A maximum reliable writing rate of 600 Hz was achieved with minimum and maximum time steps of 1661 and 1673 s, respectively, between successive data samples. To match the above SD card data writing rate, certain LSM6 control registers were changed from default values to modify sensor ranges and data rates (see table S2). In this configuration, the accelerometer range was set at the maximum value of ±16g and with the data rate of 833 Hz to ensure that the sampling rate was high enough that the data logger would log a new data point from the sensor every time.

SUPPLEMENTARY MATERIALS

robotics.sciencemag.org/cgi/content/full/3/22/eaah5228/DC1

Text

Fig. S1. Estimation of the inner diameter of a fully folded cyclic Miura-ori ring.

Fig. S2. Finite elements simulations setup.

Fig. S3. Top view of a model displaying the angles between successive external vertices.

Fig. S4. Stiffness of each model in the parametric matrix.

Fig. S5. Energy absorbed by each model in the parametric matrix.

Fig. S6. Ratio of height to width of each model in the parametric matrix.
Fig. S7. Mass of each model in the parametric matrix.
Fig. S8. Specific energy for each model in the parametric matrix.
Fig. S9. Peak reaction force for each model in the parametric matrix.
Fig. S10. Effect of the width of the most external facets (parameter E).
Fig. S11. Force and angular speed profiles at a contact angle of 60° for naked and origami-protected configuration on rough and smooth surfaces.
Fig. S12. Force and angular speed profiles at a contact angle of 30° for naked and origami-protected configuration on rough and smooth surfaces.
Fig. S13. Force and angular speed profiles at a contact angle of 60° for fixed and rotary configuration on rough and smooth surfaces.
Fig. S14. Force and angular speed profiles at a contact angle of 90° for fixed and rotary configuration on rough and smooth surfaces.
Fig. S15. Mechanical and electronic setup of the collision experiments.
Fig. S16. Manufacturing process of the Rotorigami.
Table S1. Summary of experimental results.
Table S2. Control registers for the IMU.
Movie S1. Oblique collision to a rough surface at a contact angle of 30° for the origami-protected and naked systems in the fixed and rotary configurations at 1.2 m/s (0.03×).
Movie S2. Oblique collision to a rough surface at a contact angle of 60° for the origami-protected and naked systems in the fixed and rotary configurations at 1.2 m/s (0.03×).
Movie S3. Normal collision to a rough surface for the origami-protected and naked systems in the fixed and rotary configurations at 1.2 m/s (0.03×).
Movie S4. Normal collision to a rough surface for the origami-protected system in the fixed and rotary configurations at 2 m/s (0.03×) and collisions of the aerial vehicle in the Rotorigami configuration with different obstacles during flight demonstrations.
Reference (*103*)

REFERENCES AND NOTES

1. J. Alonso-Mora, T. Naegeli, R. Siegwart, P. Beardsley, Collision avoidance for aerial vehicles in multi-agent scenarios. *Auton. Robots* **39**, 101–121 (2015).
2. X. Wang, V. Yadav, S. N. Balakrishnan, Cooperative UAV formation flying with obstacle/ collision avoidance. *IEEE Trans. Contol Syst. Technol.* **15**, 672–679 (2007).
3. H. Durrant-Whyte, N. Roy, P. Abbeel, Unmanned aircraft collision avoidance using continuous-state POMDPs, in *Robotics: Science and Systems VII* (MIT Press, 2012).
4. M. T. DeGarmo, Issues Concerning Integration of Unmanned Aerial Vehicles in Civil Airspace, MITRE Center for Advanced Aviation System Development (CAASD), McLean, Virginia, 2004.
5. S. Temizer, M. J. Kochenderfer, L. P. Kaelbling, T. Lozano-Perez, J. K. Kuchar, Collision avoidance for unmanned aircraft using Markov decision processes, in *AIAA Guidance, Navigation, and Control Conference*, Toronto, Canada, 2 to 5 August 2010, pp. 1–21.
6. A. Briod, A. Klaptocz, J.-C. Zufferey, D. Floreano, The AirBurr: A flying robot that can exploit collisions, in *2012 ICME International Conference on Complex Medical Engineering (CME)*, Kobe, Japan, 1 to 4 July 2012, pp. 569–574.
7. A. Briod, P. Kornatowski, J.-C. Zufferey, D. Floreano, A collision-resilient flying robot. *J. Field Robot.* **31**, 469–509 (2014).
8. M. Kovac, P. Sareh, Aerial Devices Capable of Controlled Flight, Patent US20180155018 (WO2016193690).
9. M. Kovač, M. Schlegel, J.-C. Zufferey, D. Floreano, Steerable miniature jumping robot. *Auton. Robots* **28**, 295–306 (2010).
10. M. Kovac, M. Schlegel, J.-C. Zufferey, D. Floreano, A miniature jumping robot with self-recovery capabilities, in *IEEE/RSJ International Conference on Intelligent Robots and Systems (IROS)*, St. Louis, MO, USA, 10 to 15 October 2009, pp. 583–588.
11. M. Kovač, The bioinspiration design paradigm: A perspective for soft robotics. *Soft Robot.* **1**, 28–37 (2013).
12. T. J. Bartelds, A. Capra, S. Hamaza, S. Stramigioli, M. Fumagalli, Compliant aerial manipulators: Toward a new generation of aerial robotic workers. *IEEE Robot. Autom. Lett.* **1**, 477–483 (2016).
13. E. Ackerman, The Secret to Small Drone Obstacle Avoidance Is to Just Crash Into Stuff (2016); https://spectrum.ieee.org/automaton/robotics/drones/the-secret-to-small-drone-obstacle-avoidance-is-to-just-crash-into-stuff.
14. M. Kovac, Learning from nature how to land aerial robots. *Science* **352**, 895–896 (2016).
15. M. Kovač, J. Germann, C. Hürzeler, R. Y. Siegwart, D. Floreano, A perching mechanism for micro aerial vehicles. *J. Micro-Nano Mech.* **5**, 77–91 (2009).
16. Y. Mulgaonkar, T. Kientz, M. Whitzer, V. Kumar, Design and fabrication of safe, light-weight, flying robots, in *ASME Int. Des. Eng.Tech. Conf. Comput. Inf. Eng. Conf.* (ASME, 2015), pp. DETC 2015–47864.
17. A. Kalantari, M. Spenko, Modeling and performance assessment of the HyTAQ, a hybrid terrestrial/aerial quadrotor. *IEEE Trans. Robot.* **30**, 1278–1285 (2014).
18. P. Kornatowski, S. Mintchev, D. Floreano, An origami-inspired cargo drone, in *IEEE/RSJ International Conference on Intelligent Robots and Systems (IROS)*, Vancouver, Canada, 24 to 28 September 2017, pp. 6855–6862.
19. X. Yang, L. M. Alvarez, T. Bruggemann, A 3D collision avoidance strategy for UAVs in a non-cooperative environment. *J. Intell. Robot. Syst.* **70**, 315–327 (2013).
20. E. N. Johnson, A. J. Calise, Y. Watanabe, J. Ha, J. C. Neidhoefer, Real-time vision-based relative aircraft navigation. *J. Aeros. Comp. Inf. Com.* **4**, 707–738 (2007).
21. G. Chowdhary, E. N. Johnson, D. Magree, A. Wu, A. Shein, GPS-denied indoor and outdoor monocular vision aided navigation and control of unmanned aircraft. *J. Field Robot.* **30**, 415–438 (2013).
22. L. Mejias, S. McNamara, J. Lai, J. Ford, Vision-based detection and tracking of aerial targets for UAV collision avoidance, in *IEEE/RSJ International Conference on Intelligent Robots and Systems (IROS)*, Taipei, Taiwan, 18 to 22 October 2010, pp. 87–92.
23. M. Odelga, P. Stegagno, H. H. Bülthoff, Obstacle detection, tracking and avoidance for a teleoperated UAV, in *IEEE International Conference on Robotics and Automation (ICRA)*, Stockholm, Sweden, 16 to 21 May 2016, pp. 2984–2990.
24. D. Scaramuzza, M. C. Achtelik, L. Doitsidis, F. Fraundorfer, E. B. Kosmatopoulos, A. Martinelli, M. W. Achtelik, M. Chli, S. A. Chatzichristofis, L. Kneip, D. Gurdan, L. Heng, G. H. Lee, S. Lynen, L. Meier, M. Pollefeys, A. Renzaglia, R. Siegwart, J. C. Stumpf, P. Tanskanen, C. Troiani, S. Weiss, Vision-controlled micro flying robots: From system design to autonomous navigation and mapping in GPS-denied environments. *IEEE Robot. Autom. Mag.* **21**, 26–40 (2014).
25. V. Kumar, N. Michael, Opportunities and challenges with autonomous micro aerial vehicles. *Int. J. Robotics Res.* **31**, 1279–1291 (2012).
26. D. Floreano, R. J. Wood, Science, technology and the future of small autonomous drones. *Nature* **521**, 460–466 (2015).
27. R. Mahony, V. Kumar, P. Corke, Multirotor aerial vehicles: Modeling, estimation, and control of quadrotor. *IEEE Robot. Autom. Mag.* **19**, 20–32 (2012).
28. J. Stowers, M. Hayes, A. Bainbridge-Smith, Biologically inspired UAV obstacle avoidance and control using monocular optical flow and divergence templates, in *International Conference on Automation, Robotics and Applications*, Wellington, New Zealand, 6 to 8 December 2011, pp. 378–383.
29. P. C. Merrell, D.-J. Lee, R. W. Beard, Obstacle avoidance for unmanned air vehicles using optical flow probability distributions, in *Proc. SPIE 5609, Mobile Robots XVII*, (2004).
30. W. E. Green, P. Y. Oh, Optic flow-based collision avoidance. *IEEE Robot. Autom. Mag.* **15**, 96–103 (2008).
31. Y. K. Kwag, C. H. Chung, UAV based collision avoidance radar sensor, in *IEEE International Geoscience and Remote Sensing Symposium*, Barcelona, Spain, 23 to 28 July 2007, pp. 639–642.
32. R. J. Fontana, E. A. Richley, A. J. Marzullo, L. C. Beard, R. W. T. Mulloy, E. J. Knight, An ultra wideband radar for micro air vehicle applications, in *IEEE Conference on Ultra Wideband Systems and Technologies*, Baltimore, MD, USA, 21 to 23 May 2002, pp. 187–191.
33. R. Sabatini, M. A. Richardson, E. Roviaro, Development and flight test of an avionics lidar for helicopter and UAV low-level flight. *J. Aeronaut. Aerospace Eng.* **2**, 114 (2013).
34. S. Modi, P. Chandak, V. Sagar Murty, E. L. Hall, A Comparison of Three Obstacle Avoidance Methods for a Mobile Robot, in *Proc. SPIE 4572, Intelligent Robots and Computer Vision XX: Algorithms, Techniques, and Active Vision* (2001).
35. N. Gageik, P. Benz, S. Montenegro, Obstacle detection and collision avoidance for a UAV with complementary low-cost sensors. *IEEE Access* **3**, 599–609 (2015).
36. J. F. Roberts, T. S. Stirling, J.-C. Zufferey, D. Floreano, quadrotor using minimal sensing for autonomous indoor flight, in *European Micro Air Vehicle Conference and Flight Competition (EMAV2007)*, Toulouse, France, 17 to 21 September 2007, pp. 1–8.
37. A. Bachrach, R. He, N. Roy, efficient planning under uncertainty for a target-tracking micro-aerial vehicle, in *Proceedings of the 28th International Conference on Machine Learning*, Bellevue, WA, USA, 2011, pp. 1–8.
38. S. Shen, N. Michael, V. Kumar, autonomous multi-floor indoor navigation with a computationally constrained MAV, in *IEEE International Conference on Robotics and Automation*, Shanghai, China, 9 to 13 May 2011, pp. 20–25.
39. M. Blosch, S. Weiss, D. Scaramuzza, R. Siegwart, Vision based MAV navigation in unknown and unstructured environments, in *IEEE International Conference on Robotics and Automation*, Anchorage, AK, USA, 3 to 7 May 2010, pp. 21–28.
40. J. M. M. Montiel, J. Civera, A. J. Davison, Unified inverse depth parametrization for monocular SLAM, in *Robotics: Science and Systems*, Philadelphia, PA, USA, 16 to 19 August 2006, pp. 1–8.
41. D. Magree, J. G. Mooney, E. N. Johnson, Monocular visual mapping for obstacle avoidance on UAVs, in *International Conference on Unmanned Aircraft Systems (ICUAS)*, Atlanta, GA, USA, 28 May 2013, pp. 471–479.
42. S. Weiss, D. Scaramuzza, R. Siegwart, Monocular-SLAM–based navigation for autonomous micro helicopters in GPS-denied environments. *J. Field Robot.* **28**, 854–874 (2011).

43. M. W. Achtelik, S. Lynen, S. Weiss, L. Kneip, M. Chli, R. Siegwart, Visual-inertial SLAM for a small helicopter in large outdoor environments, in *IEEE/RSJ International Conference on Intelligent Robots and Systems (IROS)*, Vilamoura, Portugal, 7 to 12 October 2012, pp. 2651–2652.
44. L. Doitsidis, A. Renzaglia, S. Weiss, E. Kosmatopoulos, D. Scaramuzza, R. Siegwart, 3d surveillance coverage using maps extracted by a monocular slam algorithm, in *IEEE/RSJ International Conference on Intelligent Robots and Systems (IROS)*, San Francisco, CA, USA, 25 to 30 September 2011, pp. 1661–1667.
45. Y. Mulgaonkar, A. Makineni, L. Guerrero-Bonilla, V. Kumar, Robust aerial robot swarms without collision avoidance. *IEEE Robot. Autom. Lett.* **3**, 596–603 (2018).
46. L. J. Gibson, M. F. Ashby, *Cellular Solids: Structure and Properties (Cambridge Solid State Science Series)* (Cambridge Univ. Press, 1999).
47. S. Mcvicker, *Shear Wall Basics* (2017); (http://www.mcvicker.com/vwall/page003.htm).
48. S. Felton, M. Tolley, E. Demaine, D. Rus, R. J. Wood, A method for building self-folding machines. *Science* **345**, 644–646 (2014).
49. C. D. Onal, M. T. Tolley, R. J. Wood, D. Rus, Origami-inspired printed robots. *IEEE/ASME Trans. Mechatron.* **20**, 2214–2221 (2015).
50. J. Paik, Reconfigurable materials: Algorithm for architectural origami. *Nature* **541**, 296–297 (2017).
51. S. Miyashita, S. Guitron, S. Li, D. Rus, Robotic metamorphosis by origami exoskeletons. *Sci. Robot.* **2**, eaao4369 (2017).
52. E. V. Hoff, D. Jeong, K. Lee, OrigamiBot-I: A thread-actuated origami robot for manipulation and locomotion, in *IEEE/RSJ International Conference on Intelligent Robots and Systems (IROS)*, Chicago, IL, USA, 14 to 18 September 2014, pp. 1421–1426.
53. D.-Y. Lee, S.-R. Kim, J.-S. Kim, J. J. Park, K.-J. Cho, Origami wheel transformer: A variable-diameter wheel drive robot using an origami structure. *Soft Robot.* **4**, 163–180 (2017).
54. J. Mu, C. Hou, H. Wang, Y. Li, Q. Zhang, M. Zhu, Origami-inspired active graphene-based paper for programmable instant self-folding walking devices. *Sci. Adv.* **1**, e1500533 (2015).
55. L. Paez, G. Agarwal, J. Paik, Design and analysis of a soft pneumatic actuator with origami shell reinforcement. *Soft Robot.* **3**, doi.org/10.1089/soro.2016.0023 (2016).
56. D. Rus Cynthia, C. Sung, Spotlight on origami robots. *Sci. Robot.* **3**, eaat0938 (2018).
57. A. Rafsanjani, Y. Zhang, B. Liu, Shmuel M. Rubinstein, K. Bertoldi, Kirigami skins make a simple soft actuator crawl. *Sci. Robot.* **3**, eaar7555 (2018).
58. S.-J. Kim, D.-Y. Lee, G.-P. Jung, K.-J. Cho, An origami-inspired, self-locking robotic arm that can be folded flat. *Sci. Robot.* **3**, eaar2915 (2018).
59. S. Mintchev, J. Shintake, D. Floreano, Bioinspired dual-stiffness origami. *Sci. Robot.* **3**, eaau0275 (2018).
60. C. Lv, D. Krishnaraju, G. Konjevod, H. Yu, H. Jiang, Origami based mechanical metamaterials. *Sci. Rep.* **4**, 5979 (2014).
61. J. T. B. Overvelde, T. A. de Jong, Y. Shevchenko, S. A. Becerra, G. M. Whitesides, J. C. Weaver, C. Hoberman, K. Bertoldi, A three-dimensional actuated origami-inspired transformable metamaterial with multiple degrees of freedom. *Nat. Commun.* **7**, 10929 (2016).
62. S. Babaee, J. T. B. Overvelde, E. R. Chen, V. Tournat, K. Bertoldi, Reconfigurable origami-inspired acoustic waveguides. *Sci. Adv.* **2**, e1601019 (2016).
63. R. L. Harne, D. T. Lynd, Origami acoustics: Using principles of folding structural acoustics for simple and large focusing of sound energy. *Smart Mater. Struct.* **25**, 085031 (2016).
64. R. B. Mulford, M. R. Jones, B. D. Iverson, Dynamic control of radiative surface properties with origami-inspired design. *J. Heat Transfer* **138**, 032701 (2015).
65. W. Wu, Z. You, Energy absorption of thin-walled tubes with origami patterns, in *5th International Meeting on Origami in Science, Mathematics and Education (5OSME)*, Singapore, 13 to 17 July 2010, pp. 277–290.
66. J. Song, Y. Chen, G. Lu, Axial crushing of thin-walled structures with origami patterns. *Thin-Walled Struct.* **54**, 65–71 (2012).
67. S. H. Min C.C., Geometrical properties of paper spring, in *Manufacturing Systems and Technologies for the New Frontier* (Springer, 2008).
68. J. Ma, Z. You, Energy absorption of thin-walled square tubes with a prefolded origami pattern—Part I: Geometry and numerical simulation. *J. Appl. Mech.* **81**, 011003 (2014).
69. K. Terada, K. Kadoi, S. Tokura, T. Sushida, I. Hagiwara, The deformation mechanism on origami-based foldable structures. *Int. J. Vehicle Performance* **3**, 334–346 (2017).
70. F. Haas, R. J. Wootton, Two basic mechanisms in insect wing folding. *Proc. R. Soc. Lond., B, Biol. Sci.* **263**, 1651–1658 (1996).
71. F. Haas, Wing folding in insects: A natural, deployable structure, in *IUTAM-IASS Symposium on Deployable Structures: Theory and Applications*, Cambridge, UK, 6 to 9 September 2000, pp. 137–142.
72. A. K. Stowers, D. Lentink, Folding in and out: Passive morphing in flapping wings. *Bioinspir. Biomim.* **10**, 025001 (2015).
73. L. Dufour, K. Owen, S. Mintchev, D. Floreano, A drone with insect-inspired folding wings, in *IEEE/RSJ International Conference on Intelligent Robots and Systems (IROS)*, Daejeon, South Korea, 9 to 14 September 2016, pp. 1576–1581.
74. P. Sareh, P. Chermprayong, M. Emmanuelli, H. Nadeem, M. Kovac, The spinning cyclic 'Miura-oRing' for mechanical collision-resilience, in *The 7th International Meeting on Origami in Science, Mathematics and Education (7OSME)*, Oxford, UK, 5 to 7 September 2018, pp. 981–994.
75. K. Miura, Map fold a La Miura style, its physical characteristics and application to the space science, in *Research of Pattern Formation*, R. Takaki, Ed. (KTK Scientific Publishers, 1994), pp. 77–90.
76. K. Miura, The science of Miura-ori: A review, in *Fourth International Conference on Origami in Science, Mathematics, and Education (4OSME)*, Pasadena, CA, USA, 8 to 10 September 2006, pp. 87–99.
77. P. Sareh, Symmetric Descendants of the Miura-ori, PhD dissertation, Engineering Department, University of Cambridge, UK (2014).
78. K. Miura, in *Method of Packaging and Deployment of Large Membranes in Space* (Institute of Space and Astronautical Science, 1985), vol. 618, pp. 1–9.
79. T. Tachi, Generalization of rigid-foldable quadrilateral-mesh origami, in *Proceedings of the International Association for Shell and Spatial Structures (IASS)*, Valencia, Spain, 28 September to 2 October 2009, pp. 2287–2294.
80. Y. Klett, K. Drechsler, Designing technical tessellations, in *5th International Meeting on Origami in Science, Mathematics and Education (5OSME)*, Singapore, 13 to 17 July 2010, pp. 305–322.
81. R. J. Lang, A. Bateman, Every spider web has a simple flat twist tessellation, in *5th International Meeting on Origami in Science, Mathematics and Education (5OSME)*, Singapore, 13 to 17 July 2010, pp. 455–473.
82. T. Hahn, *International Tables for Crystallography, Volume A: Space-group Symmetry* (Springer, 2005).
83. P. Sareh, S. D. Guest, A Framework for the symmetric generalisation of the Miura-ori, in *International Journal of Space Structures, Special Issue on Folds and Structures* (Multi-Science Publishing Co Ltd., 2015).
84. P. Sareh, S. D. Guest, Minimal isomorphic symmetric variations on the Miura fold pattern, in *The First International Conference on Transformable Architecture (Transformable 2013)*, Seville, Spain, 18 to 20 September 2013, pp. 313–318.
85. P. Sareh, S. D. Guest, Designing symmetric derivatives of the Miura-ori, in *Advances in Architectural Geometry*, P. Block, J. Knippers, N. Mitra, W. Wang, Eds. (Springer, 2014), pp. 233–241.
86. P. Sareh, S. D. Guest, Design of isomorphic symmetric descendants of the Miura-ori. *Smart Mater. Struct.* **24**, 085001 (2015).
87. P. Sareh, S. D. Guest, Tessellating variations on the Miura fold pattern, in *IASS-APCS Symposium*, Seoul, South Korea, 21 to 24 May 2012, pp. 1070–1078.
88. P. Sareh, S. D. Guest, Design of non-isomorphic symmetric descendants of the Miura-ori. *Smart Mater. Struct.* **24**, 085002 (2015).
89. R. L. E. Schwarzenberger, The 17 plane symmetry groups. *Math. Gazette* **58**, 123–131 (1974).
90. P. T. Barreto, Lines meeting on a surface: The "MARS" paperfolding, in *Origami Science and Art: Proceedings of the Second International Meeting of Origami Science and Scientific Origami*, K. Miura, Ed. (Seian University of Art and Design, Otsu, Shiga, 1997), pp. 343–359.
91. T. Nojima, Modelling of folding patterns in flat membranes and cylinders by origami. *JSME Int. J. Ser. C* **45**, 364–370 (2002).
92. T. Hull, R. Lang, R. Schamp, Pleated multi-sliced cone, in *The 2012 Joint Mathematics Meetings*, Boston, MA, USA, 4 to 7 January 2012.
93. R. J. Lang, Oval Tessellation; http://www.langorigami.com/crease-pattern/oval-tessellation.
94. M. Bischoff, K.-U. Bletzinger, W. A. Wall, E. Ramm, Models and finite elements for thin-walled structures, in *Encyclopedia of Computational Mechanics*, E. Stein, R. de Borst, T. J. R. Hughes, Eds. (John Wiley & Sons Ltd., 2004).
95. G. Lu, T. Yu, *Energy Absorption of Structures and Materials* (Woodhead Publishing Ltd. and CRC Press LLC, 2003).
96. A. G. Mamalis, W. Johnson, The quasi-static crumpling of thin-walled circular cylinders and frusta under axial compression. *Int. J. Mech. Sci.* **25**, 713–732 (1983).
97. W. Johnson, *Crashworthiness of Vehicles* (Institution of Mechanical Engineers, 1978).
98. L. Zheng, T. Wierzbicki, Quasi-static crushing of S-shaped aluminum front rail. *Int. J. Crashworthiness* **9**, 155–173 (2004).
99. T. Børvik, O. S. Hopperstad, A. Reyes, M. Langseth, G. Solomos, T. Dyngeland, Empty and foam-filled circular aluminium tubes subjected to axial and oblique quasistatic loading. *Int. J. Crashworthiness* **8**, 481–494 (2003).
100. N. Jones, *Structural Impact* (Cambridge Univ. Press, 1997).
101. https://github.com/pololu/lsm6-arduino.
102. https://github.com/greiman/SdFat.
103. Simulia, Abaqus Analysis User's Manual (Abaqus 6.12), Simulia Corp., 2012.

Acknowledgments: We are thankful to R. Hutchins, M. Grant, and A. Smith of the Mechanical and Technology Workshops at the Aeronautics Department of Imperial College

London for invaluable technical support and to G. Baker for assistance with the development of moment-decoupling protectors. We are also thankful to S. Sareh, A. Panesar, and R. Siddall for useful comments. Any findings presented in this paper are those of the authors and do not necessarily express those of the funding bodies. **Funding:** The research presented in this study was funded by the Engineering and Physical Sciences Research Council (EP/ K503733/1) and by the Department of Aeronautics at Imperial College London, UK. **Author contributions:** P.S. and M.K. invented and developed the concept (patented via Imperial Innovations). P.S. designed, developed, and manufactured the Rotorigami. M.E. carried out finite element modeling and analysis. P.S., P.C., and H.N. designed and carried out the experiments and data analyses. P.C. developed electronic measurement systems. All authors discussed and interpreted the results. **Competing interests:** P.S.and M.K. are inventors on patent application PCT/GB2016/051567 (EP20160726640 20160527) submitted by Imperial Innovations that covers the concept of Rotorigami presented in this paper. The other authors declare that they have no competing interests. **Data and materials availability:** All data needed to support the conclusions are presented in the main text or the Supplementary Materials.

Submitted 8 March 2018
Accepted 5 September 2018
Published 26 September 2018
10.1126/scirobotics.aah5228

Citation: P. Sareh, P. Chermprayong, M. Emmanuelli, H. Nadeem, M. Kovac, Rotorigami: A rotary origami protective system for robotic rotorcraft. *Sci. Robot.* **3**, eaah5228 (2018).

Science Robotics

Rotorigami: A rotary origami protective system for robotic rotorcraft

Pooya Sareh, Pisak Chermprayong, Marc Emmanuelli, Haris Nadeem and Mirko Kovac

Sci. Robotics **3**, eaah5228.
DOI: 10.1126/scirobotics.aah5228